PAPER

Probing the dynamic response of antivortex, interstitial and trapped vortex lattices on magnetic periodic pinning potentials

Supercond. Sci. Technol. **26** (2013) 085018 (8pp) doi:10.1088/0953-2048/26/8/085018

Probing the dynamic response of antivortex, interstitial and trapped vortex lattices on magnetic periodic pinning potentials

A Gomez[1], E M Gonzalez[1,2], D A Gilbert[3], M V Milošević[4], Kai Liu[3] and J L Vicent[1,2]

[1] Departamento de Física de Materiales, Facultad de Ciencias Fisicas, Universidad Complutense, E-28040 Madrid, Spain
[2] IMDEA-Nanociencia, Cantoblanco, E-28049 Madrid, Spain
[3] Department of Physics, University of California, Davis, CA 95616, USA
[4] Departement Fysica, Universiteit Antwerpen, Groenenborgerlaan 171, B-2020 Antwerpen, Belgium

E-mail: jlvicent@fis.ucm.es

Received 10 April 2013, in final form 3 June 2013
Published 2 July 2013
Online at stacks.iop.org/SUST/26/085018

Abstract
The dynamics of the pinned vortex, antivortex and interstitial vortex have been studied in superconducting/magnetic hybrids consisting of arrays of Co/Pd multilayer nanodots embedded in Nb films. The magnetic nanodots show out-of-plane magnetization at the remanent state. This magnetic state allows for superconducting vortex lattices of different types in an applied homogeneous magnetic field. We experimentally and theoretically show three such lattices: (i) a lattice containing only antivortices; (ii) a vortex lattice entirely pinned on the dots; and (iii) a vortex lattice with pinned and interstitial vortices. Between the flux creep (low vortex velocity) and the free flux flow (high vortex velocity) regimes the interaction between the magnetic array and the vortex lattice governs the vortex dynamics, which in turn enables distinguishing experimentally the type of vortex lattice which governs the dissipation. We show that the vortex lattice with interstitial vortices has the highest onset velocity where the lattice becomes ordered, whereas the pinned vortex lattice has the smallest onset velocity. Further, for this system, we directly estimate that the external force needed to depin vortices is 60% larger than the one needed to depin antivortices; therefore we are able to decouple the antivortex–vortex motion.

(Some figures may appear in colour only in the online journal)

1. Introduction

Superconducting vortices are the ideal tool for studying a broad variety of phenomena such as soft matter phase transitions [1] and ratchet effects [2]. They can be considered as soft-core 'particles', and on tailoring the experimental system, can be used to gain a better insight into many areas of research. One such example is the dynamics of interacting particles moving in energy landscapes. Typically the landscapes are generated by: (i) intrinsic and random defects present in the sample; or (ii) artificially structured pinning sites, which can be fabricated randomly [3] or in regular arrays [4]. One of the most remarkable properties of vortices is that their quantity and physical characteristics can be tuned externally, for example, by means of an applied magnetic field or temperature. In addition, the particle behavior can be modified by adjusting the pinning landscapes.

Hybrid structures made of magnetic arrays embedded in superconducting films provide an ideal platform for tailoring the vortex dynamic properties, by nanoengineering the size,

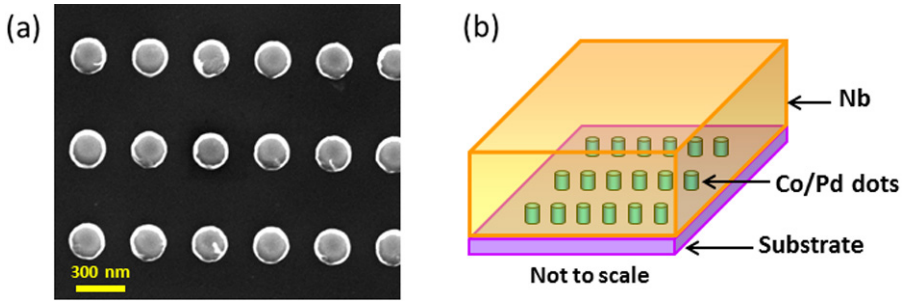

Figure 1. (a) Scanning electron microscopy image of the array (the scale bar corresponds to 300 nm). (b) Schematic of the sample with an array of magnetic nanodots embedded in the Nb superconducting film.

geometry, or magnetization of the magnetic lattice. In recent years, stimulating results have been reported in this area; see [5, 6]. Vortex lattice velocity is one of the key parameters that have been studied for these hybrid nanostructures, and it was found to exhibit several interesting properties. For example, Silhanek *et al* [7] have found a deviation from the well-known model of Larkin and Ovchinnikov [8] in the high vortex velocity regime v^* (when the flux flow dissipation undergoes an abrupt transition to the normal state for currents higher than a current J^*). On the other hand, a completely different insight into vortex dynamics can be obtained from the low vortex velocity regime, close to the critical current density J_c (when the vortex lattice depins and starts moving) and well below J^*. In this low current approach, flux creep of vortices is strongly governed by the field polarity of the nanodots [9, 10]. Recently, also in the low velocity regime, Kramer *et al* [11] have studied the vortex–antivortex behavior by scanning Hall microscopy. They reported that the antivortices can be shaken by small ac field excitation, while the vortices sitting on top of the magnetic structures remain at rest. In other words, they demonstrated that antivortices could be more easily subjected to motion than the vortices. In the present work we differentiate between different kinds of vortices (vortices at pinning sites, vortices between pinning sites and antivortices), and show that they move at different velocities. Furthermore, we establish a quantitative comparison of the depinning forces necessary to set the different kinds of vortices in motion. In doing so, we distinguish experimentally the dominant type of vortices in the dissipation process.

The paper is organized as follows. We first present the experimental details on sample fabrication, magnetic characterization and magneto-transport measurement methods. A theoretical model based on the non-linear Ginzburg–Landau theory is then introduced. Sections 2 and 3 address the theoretical and experimental results and the analysis of different classes of vortices and their mobility. Finally, our findings are summarized in section 4.

2. The experimental method and theoretical model

Arrays of circular Co/Pd nanodots (230 nm diameter and 42 nm thickness, shown in figure 1(a)) were fabricated on Si(100) substrates, using electron beam lithography and the lift-off technique in combination with DC magnetron sputtering in an ultrahigh vacuum chamber with a base pressure of 1×10^{-8} Torr. The nanodots are polycrystalline, arranged on a rectangular lattice (400 nm $\times$ 600 nm spacing) covering an area of 100 μm $\times$ 100 μm. The dots consist of a $[\mathrm{Pd}(0.6\ \mathrm{nm})/\mathrm{Co}(0.4\ \mathrm{nm})]_{40}$ multilayer, deposited in 12 mTorr Ar atmosphere, with a 2 nm Pd capping layer to prevent oxidation. Samples grown with these parameters have been previously shown to exhibit a perpendicular anisotropy [12, 13].

Magnetic characterizations were performed using vibrating sample magnetometry (VSM) at room temperature to confirm the remanent magnetic configurations of the Co/Pd samples. Magnetic force microscopy (MFM) was performed using a low moment CoCr coated cantilever in phase detection mode. Scanning electron microscopy (SEM) was also performed to study the nanodot morphology.

After the magnetic characterization, a 100 nm thick Nb film was deposited by magnetron sputtering on top of the magnetic dots, forming the magnetic/superconductor hybrid structure (see the schematic in figure 1(b)). Standard photolithography and ion etching techniques were used to define a cross-shaped, 40 μm bridge centered on the array to carry out the magneto-transport study. A commercial helium cryostat with variable temperature insert and a superconducting solenoid was used for the measurements. Small magnetic fields (up to 1 kOe) were applied perpendicularly to the sample plane, which do not alter the remanent magnetic state of the nanodots.

To complement the experimental study, we performed a theoretical analysis using the non-linear Ginzburg–Landau (GL) formalism. Since we are dealing with a type-II superconductor thin film, the formalism reduces to solving the following equation:

$$(-\mathrm{i}\nabla - A)^2\psi = (1 - T - |\psi|^2)\psi, \qquad (1)$$

where A denotes the vector potential resulting from the total applied magnetic field H (consisting of the stray field $\vec{h}_m$ generated by the nanomagnets and the applied perpendicular magnetic field $\vec{H}_a$, i.e., $\mathrm{rot}\vec{A} = \vec{H} = \vec{h}_m + \vec{H}_a$), ψ is the superconducting order parameter, and T is the temperature scaled to the critical temperature $T_c = 8.71$ K. Generally speaking, the physics of superconductor–ferromagnet hybrids is often affected by the proximity effect, which is neglected in equation (1). However, such effects can be accounted for by

adequately estimated suppression of superconductivity, which can be included in equation (1) via spatially varying T_c. We solve equation (1) iteratively by adding a time derivative of ψ on the left side of the equation, where each step of iteration corresponds to the GL time $t_0 = \pi\hbar/8k_BT_c$. The relaxed numerical solution of equation (1) minimizes the free energy:

$$\mathscr{G}/\mathscr{G}_0 = V^{-1}\int -|\psi|^4\,dV, \qquad (2)$$

where $\mathscr{G}_0$ equals the superconducting condensation energy ${H_c}^2/8\pi$ and V is the volume of the sample. In equations (1) and (2), the distances are expressed in units of the coherence length $\xi_0 = \xi(T = 0)$, the vector potential is scaled to $\Phi_0/2\pi\xi_0$ (where Φ_0 is the flux quantum), and the order parameter is scaled to its bulk value in the absence of field and for zero temperature. The equation is solved in a rectangular simulation region $w_x \times w_y$ (800 nm × 1200 nm) with periodic boundary conditions (so in practice an infinite film is studied).

To explore the superconducting state, we initialize the calculations from the zero-field cooled state ($H_a = 0$) and $\psi = 1$. The magnetization of the dots can then be gradually increased, and the ground state obtained for the previously considered magnetization is used as the new initial condition for recalculating the vortex structure. This process is repeated with decreasing magnetization [14, 15], and in minor loops for all vortex states found. Finally, a whole collection of possible vortex configurations is obtained, and the ground state is determined by comparing the energies of all stable states. However, this procedure is different for the applied homogeneous magnetic field (non-zero H_a). This field cannot be gradually changed, as correct implementation of the periodic boundary conditions requires the flux through the simulation region to be an integer multiple of a flux quantum Φ_0 [16]. Thus the procedure for fixed magnetization of the dots but for varied external magnetic field is the same as that described above, but the increments/decrements of the applied field are discrete and determined by flux quantization.

3. Results and discussion

Prior to Nb deposition, magnetic characterization was performed. Figure 2 shows the out-of-plane and in-plane hysteresis loops of a reference sample and confirms the out-of-plane anisotropy [17, 18]. The remanent state of the magnetic dots is achieved by applying a 20 kOe saturating magnetic field perpendicular to the substrate and then switching it off. The nanodots exhibit a single-domain state at remanence after saturation. The stray field generated by the dots has been calculated, and is presented in the inset in figure 2.

Once the magnetic characterization was performed, we analyzed the influence of these magnetic nanodots on the vortex lattice dynamics. Magneto-transport measurements have been used to probe the vortex lattice behavior in the low velocity regime. In our hybrid samples the vortex lattice moves on two different pinning landscapes: (i) random pinning potentials generated by intrinsic defects in the sample; and (ii) periodic and ordered pinning potentials generated

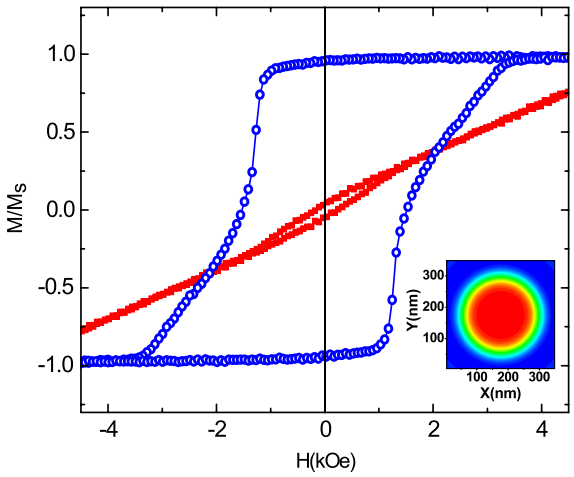

Figure 2. Out-of-plane (blue circles) and in-plane (red squares) hysteresis loop obtained for a reference sample of the $[Pd(0.6\ nm)/Co(0.4\ nm)]_{40}$ film. The inset shows the magnetic stray field profile generated by each magnetic dot, in a plane 50 nm above the dot.

by the Co/Pd magnetic dots. The competition between these potentials governs the vortex lattice's dynamic response. Two extreme regimes can be expected, taking into account low and high applied currents: (i) driving currents quite close to the critical current; and (ii) at much higher driving currents. In the former regime, for very low velocities, the intrinsic random pinning overcomes the periodic pinning potentials [19]. In the latter regime, the vortex lattice moves at very high velocities and the interactions between the pinning centers and the vortex lattice can be neglected. In this regime, the force (current) versus velocity (voltage) is linear and the vortices move in a free flux flow. In between those two regimes the competition between the random and the ordered pinning governs the vortex dynamics. This work focuses exactly on this region of competing pinning interactions, specifically in the narrow temperatures and driving force window where the artificial (ordered) pinning governs the vortex lattice behavior [19]. In this intermediate regime, a rich vortex dynamics phenomenology [5] can be studied, e.g., effects of commensurability between the vortex lattice and the array of pinning centers [20], reconfiguration of the vortex lattice [21], channeling effects [22], etc.

Figure 3(a) shows the magnetoresistance data obtained at $T = 0.99T_c$, for the hybrid sample with $[Pd(0.6\ nm)/Co(0.4\ nm)]_{40}$ multilayer nanodots. Note that, as shown previously, the dependence of the resistance on the magnetic field is very different depending on whether the applied magnetic field corresponds to matching condition or not [20]. If the vortex density is an integer multiple of the pinning center density ($H = nH_{match}$) [23], the vortex and the pinning lattices are commensurate and the vortex lattice is strongly affected by the periodic pinning potential which slows down the vortex motion. As seen in figure 3(a), this manifests as well defined, equally spaced, sharp minima in the magnetoresistance.

The results shown in figure 3(a) correspond to two configurations of the remanent state: one with the positive remanent magnetization ($m_z > 0$) obtained with the saturating

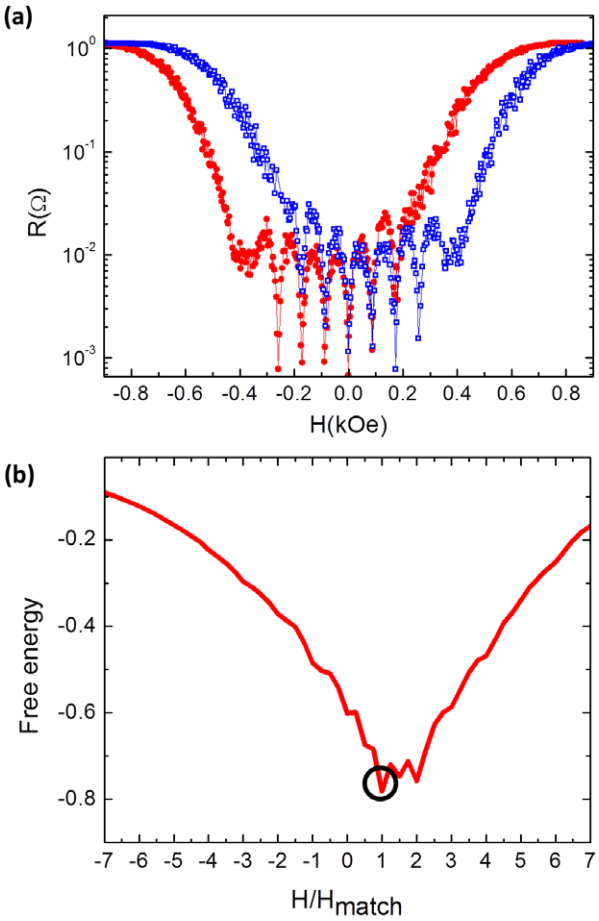

Figure 3. Resistance (R) as a function of the magnetic field (H) at $T = 0.99T_c$ with $I = 3$ mA and $T_c = 8.71$ K. Red filled circles correspond to the curve obtained for negative remanent magnetization and blue hollow squares to the positive remanent magnetization. Figure 2(b) shows the Gibbs free energy as a function of the external magnetic field.

field in the positive direction, and the other for the negative saturating field ($m_z < 0$). The periodic minima distribution shows a clear asymmetry around H_{match} ($-H_{match}$) for the positive (negative) remanent configuration, with more minima observed when the magnetic moment lies parallel to the external magnetic field (in positive fields for the $m_z > 0$ configuration and in negative fields for $m_z < 0$ configuration).

This observed asymmetry can be due to two different origins. On one hand, the pinning strength depends on the relative alignment between the magnetic moments of the dots and the external applied magnetic field [24]. If the polarity of the superconducting vortex and the magnetization of the dot are parallel, the vortex is attracted by the dot [10]. The opposite occurs if the two are in opposite directions; the superconducting vortex is repelled by the magnetic dot and resides at interstitial positions between the dots. The second possible origin is the nucleation of vortex–antivortex (V–AV) pairs by the magnetic dots [14]. In this case, the asymmetry is produced by the annihilation of one of them by the external magnetic field [25].

To determine the origin of the observed asymmetry in the magnetoresistance curves shown in figure 3(a), we perform a theoretical study of our system at $T = 0.99T_c$. For that, we use the GL formalism explained above to simulate a 100 nm thick Nb film ($\xi_0 = 9$ nm [26]) grown on top of a rectangular array (400 nm × 600 nm) of out-of-plane magnetized Co nanodots (40 nm thick and 230 nm diameter) with positive magnetization ($m_z > 0$). The Co saturation magnetization was rescaled from 1400 to 560 G (16 nm of Co out of 40 nm total thickness) to simulate the average magnetization of the Co/Pd multilayer structure of the nanodots.

To begin with, we analyze the calculated free energy versus the magnetic field normalized to the first matching field (H_{match}; figure 3(b)). A clear asymmetry is observed around $+H_{match}$ and it is in agreement with the experimental results shown in figure 3(a). The global minimum of the free energy—highlighted by a circle—is reached at the first positive matching field. This minimum proves that states with vortices have lower energy than those without them. This may be due to two reasons: (1) the energetically favorable compensation of the vortex currents and the screening currents over the dots (where vortices are pinned); and (2) the nucleation of a V–AV pair over each dot and subsequent annihilation of antivortices with vortices due to external field. To clarify the underlying mechanism for this phenomenon, we calculate and visualize the nucleation and stabilization of vortex states in our system.

The non-linear Ginzburg–Landau (GL) theory is a very useful tool for revealing the actual vortex lattice configuration, since it allows for a nonuniform distribution of the superconducting order parameter $\Psi(\mathbf{r})$; i.e. vortex cores can be imaged in this numerical experiment at locations where the order parameter drops to zero, and its phase has a whirl of 2π. Using the GL approach we obtained the ground state configuration for different numbers of vortices per unit cell, i.e. under different (fractional and integer) matching fields. Figure 4 shows the contour plots of the Cooper pair density of the ground state vortex configurations obtained for a magnetic array of dots with positive magnetization ($m_z > 0$) for different values of the applied magnetic field ranging from (a) $H = -H_{match}$, i.e. the first negative matching field, to (l) $H = 4H_{match}$, i.e. for applied field four times the value of the first matching field.

Figure 4(e) shows the contour plot configuration obtained for $H = 0$. It is clear that no V–AV pairs are induced in the sample, probably because they cannot be separated and stabilized since the magnetic lattice is too dense compared to the coherence length at this temperature ($\xi(0.99T_c)$) [14]. However, figures 4(d) and (f) show that under a small applied magnetic field ($H = \pm 0.25H_{match}$), V–AV pairs are induced in the system as was predicted earlier in [27]. This suggests that vortex–antivortex creation and annihilation processes are essential in the analysis of the energy spectrum of the superconducting state of the system considered. Therefore, in figure 5 we show the simulated antivortex annihilation by the external magnetic field. State (a) corresponds to the vortex configuration obtained for $H = 0.75H_{match}$, for which one antivortex is placed in the interstitial position in the field of view shown. Then, the external vortex induced by the applied magnetic field enters the observed area (states (b) and (c)), until it annihilates with the existing antivortex

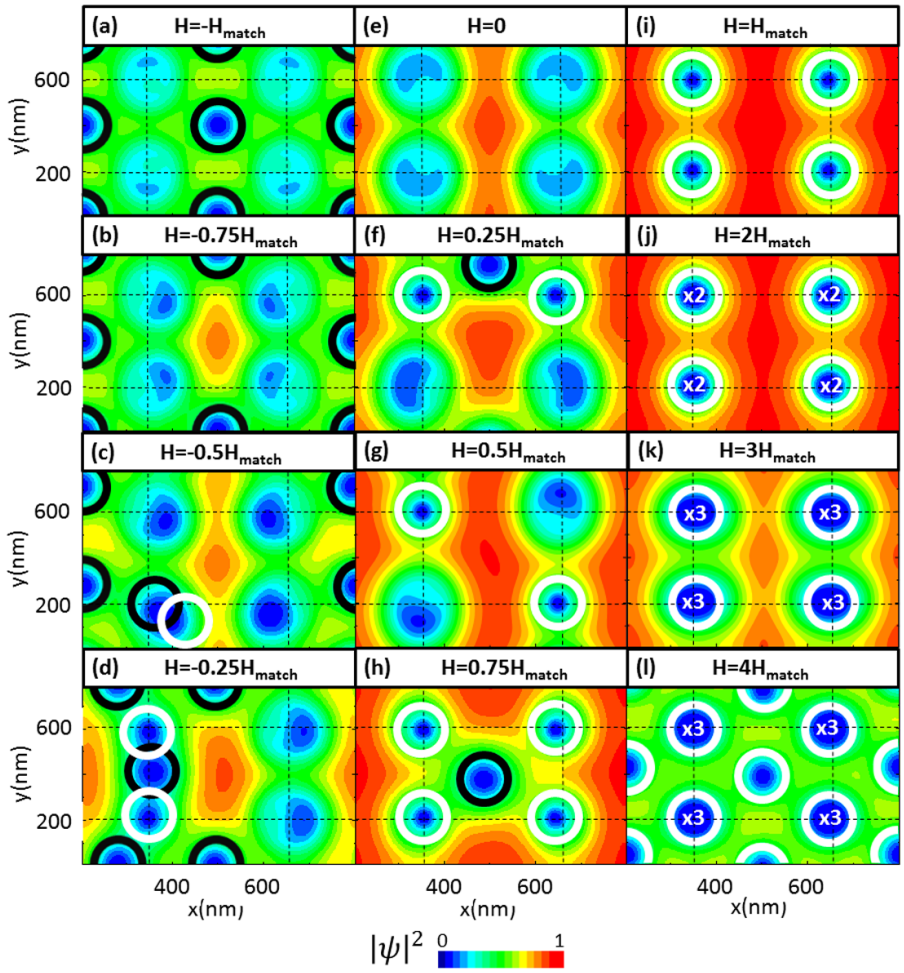

Figure 4. Contour plots of the Cooper pair density for the ground state vortex configurations obtained in a sample with positive magnetic remanent state of the nanodots, for different external applied magnetic fields: from $H = -H_{\text{match}}$ (a) to $H = 4H_{\text{match}}$ (l). Blue/red color corresponds to low/high Cooper pair density, white/black circles show the positions of the vortices/antivortices and dashed lines indicate the unit cells of the periodic lattice of nanodots.

(state (d)) and the ground state is obtained. Therefore, the optimal superconductivity is obtained for $H = H_{\text{match}}$ (where a minimum in the free energy is found (figure 2(b))) due to the most favorable compensation of currents in the system (i.e. minimized supercurrents due to compensation of Meissner currents over the dots by currents of vortices sitting on the dots), but also due to the annihilation of any remaining interstitial antivortices for $H < H_{\text{match}}$.

In summary, for $H = H_{\text{match}}$ only vortices on top of the dots are obtained: the external magnetic field annihilates the antivortices generated by the magnetic dots and only vortices are established in the ground state. For higher matching fields, $2H_{\text{match}}$ and $3H_{\text{match}}$, more vortices are pinned on the dots, they coalesce into a giant vortex (with vorticity 2 and 3 respectively) [28]. The opposite process occurs for $H = -H_{\text{match}}$, in which case the external magnetic field annihilates the vortices placed on top of the dots and an antivortex lattice is established at the interstitial positions of the array, while dots remain vortex-free. This state is unstable under an applied drive since interstitial antivortices are very loosely bound to the dots.

Finally, we point out one more particular state, namely for $H = 4H_{\text{match}}$, where we find that a three-quanta giant vortex is placed on top of the dots and an extra vortex appears in the interstitial position of the dot array. This can be seen in the magnetoresistance curves shown in figure 3, where the

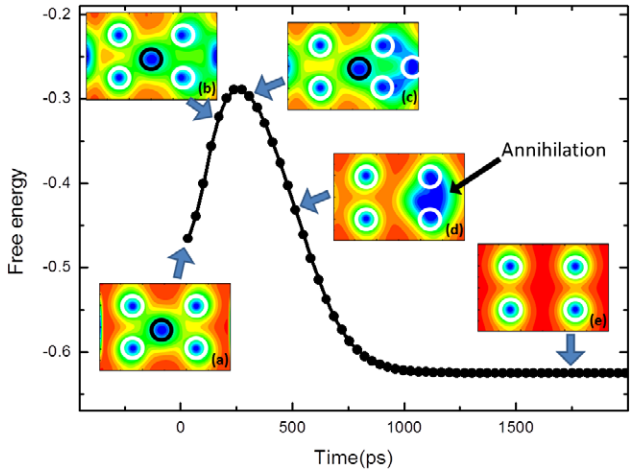

Figure 5. Antivortex annihilation process for $H = H_{\text{match}}$. Inset (a) shows the initial state, which corresponds to $H = 0.75H_{\text{match}}$ (figure 3(h)). Insets (b)–(d) show the snapshots of the annihilation process and inset (e) shows the final state.

fourth minimum is much shallower and less defined than the first three minima. This is a fingerprint indicating that the fourth minimum corresponds to a vortex configuration in which an interstitial vortex appears as shown in figure 4(l). Dots of similar dimensions tend to a vortex occupation number of 1 [29], but, in the present case, the out-of-plane magnetization of the dots increases the filling factor up to 3 [11]. This increase in the filling factor is the reason that no vortex reconfiguration is observed in our magnetoresistance curves contrary to what is observed for Ni dots of similar dimensions [21]. Finally we note that in our calculations the proximity effect was not taken into account, although in principle it can affect the filling factor. We have checked this by suppressing superconductivity above all dots, only to realize that it has no consequence for any of the above reported phenomena. At the same time, the suppression due to proximity prevents one from observing the peculiarities of the vortex states (as e.g. shown in figure 4), so we opted to disregard the proximity effect in all figures presented.

From the above results we conclude that the combination of suitable magnetic pinning potentials and appropriate applied magnetic fields (number of vortices in the unit cell of the array) allows discrimination between different kinds of vortices in the sample, so commensurability effects become a tool for distinguishing between different kinds of vortices and studying their dynamics.

To study the vortex lattice dynamics we perform the following experimental procedure. First, we apply the appropriate magnetic field to establish a certain vortex configuration and we keep it constant. Then, we apply a current density $\vec{J}$, which yields a Lorentz force on the vortices, $\vec{F}_{\rm L} = \vec{J} \times \vec{n}\Phi_0$, where $\vec{n}$ is the unit vector along the field direction. Above the threshold current, this force sets the vortex lattice into motion with average velocity $\vec{v}$. Force–velocity curves ($F_{\rm L}$ versus v) can be extracted from the experimental I–V characteristics by calculating the Lorentz force and using the Josephson relation for the electric field $\vec{E} = \vec{B} \times \vec{v}$. Force–velocity curves measured at two different fields: at matching field $H_{\rm match}$ and at a smaller field value $H_{\rm outmatch}$ close to $H_{\rm match}$ but far enough away to be out of matching conditions have been obtained to extract the force enhancement $\Delta F_{\rm L} = F_{\rm L\ matching} - F_{\rm L\ out\ of\ matching}$. This is a measure of the driving force enhancement at matching conditions where a vortex lattice is moving with long range order induced by the ordered potential landscape [19]. In addition, by plotting $\Delta F_{\rm L}$ versus the vortex lattice velocity we can detect the velocity range for which the interaction between the ordered pinning and the different kinds of vortices is observable.

We have chosen three experimental conditions for exploring the relevant dynamics: (i) the antivortex lattice, i.e. one interstitial antivortex per unit cell, placed in its center (figure 4(a)); (ii) the trapped single-vortex lattice, i.e. a single vortex sitting on each dot (figure 4(i)); and (iii) a vortex lattice with a trapped giant vortex and a single interstitial vortex, i.e. a giant vortex at each dot and one interstitial vortex in the center of the unit cell (figure 4(l)). Figure 6 shows the results for the three situations considered: an isolated antivortex (circles),

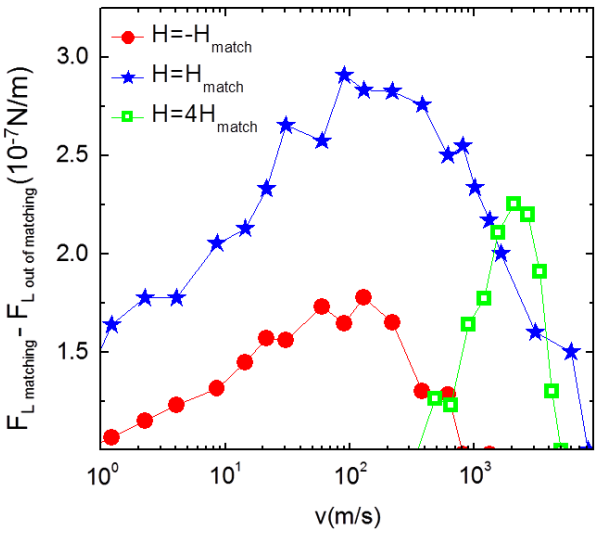

Figure 6. Force enhancement ($\Delta F_{\rm L} = F_{\rm L\ matching} - F_{\rm L\ out\ of\ matching}$) as a function of the vortex lattice velocity at $0.99T_{\rm c}$. Red circles show the pinning enhancement for $H = -H_{\rm match}$, blue stars that for $H = H_{\rm match}$ and green squares that for $H = 4H_{\rm match}$.

vortices placed on the dots (stars), and finally interstitial and pinned vortices (squares).

First of all, we observe that the vortex dynamics are sensitive to the type of vortex which is moving. Taking into account that the highest value of $\Delta F_{\rm L}$ indicates the most ordered moving lattice [19], the vortex lattice consisting of 'pinned' vortices shows an enhancement in their interaction with the pinning landscapes. This is indicative of the strong attractive interaction between a vortex line and a magnetic moment aligned parallel to it and it places it in the largest vortex velocity interval where the order occurs. On the other hand, the motion of antivortices ($H = -H_{\rm match}$) can be considered as scaled down in comparison with that of the vortices ($H = H_{\rm match}$). In this case, the antivortices experience a repulsive interaction with the magnetic dots and the origin of the pinning is a 'caging effect'. This interaction results in a weaker pinning, and a $\Delta F_{\rm L}$ reduction is observed. In addition, the velocity interval where the ordering takes places is reduced.

Finally, we have studied the results obtained for the vortex lattice with interstitial vortices ($H = 4H_{\rm match}$ in figure 4(l)). In this case, the interaction between the pinned vortices and the interstitial vortices makes the vortex lattice stiffer and the onset velocity is shifted to higher values and, at the same time, the velocity interval where the moving lattice is ordered has shrunk.

These results shed light on other key vortex dynamics issues, which are the evaluation of the forces necessary to move a vortex or an antivortex lattice and quantification of the difference in the pinning strength. Figure 7 shows the experimental results obtained using the normalized Lorentz force difference $(F_{{\rm L}n=+1} - F_{{\rm L}n=-1})/(F_{{\rm L}n=-1})$, where $F_{{\rm L}n=+1}$ and $F_{{\rm L}n=-1}$ are the Lorentz forces needed to move the vortex and antivortex lattices at a certain velocity, respectively. We observe that the force needed to start moving the vortex

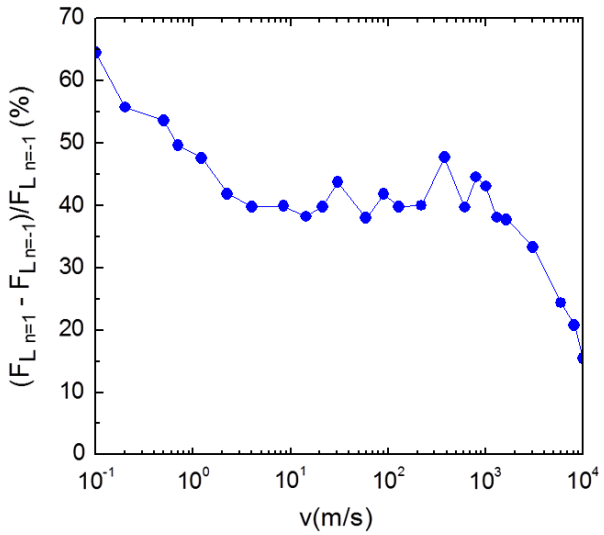

Figure 7. Velocity dependence of the normalized difference of the Lorentz force needed to move a vortex and an antivortex $((F_{Ln=+1} - F_{Ln=-1})/F_{Ln=-1})$ at $T = 0.99T_c$. Note that the force needed to start moving a vortex is 65% higher than that needed to start moving an antivortex. Once they are moving, the difference is 40% until the velocity is high enough that interaction between the vortex lattice and pinning array is overcome.

lattice is 65% higher than that for the antivortex. Once they are moving, the difference plateaus at 40% over a range in velocity spanning three orders of magnitude. When the velocity is high enough that the interaction between the vortex/antivortex lattice and the pinning array is overcome and the free flux flow regime is reached, this difference vanishes.

4. Conclusions

In summary, vortex states in a Nb film with embedded arrays of magnetic nanodots have been studied. We show that by applying a small external magnetic field, vortex–antivortex pairs can be induced in the sample, which results in a plethora of possible vortex configurations as a function of the applied field. Using the commensurability effect, i.e. selecting the appropriate magnetic field, three different kinds of periodic lattices have been established in the sample: (i) the pure antivortex lattice; (ii) the vortex lattice with all vortices pinned on the dots; and (iii) the vortex lattice with pinned and interstitial vortices. The dynamics of these three different vortex lattices have been explored. The pinned vortex lattice shows the most robust response with the broadest velocity window (the vortices remain as an ordered lattice between 1 and 10^4 m s^{-1}) and the strongest interaction between the periodic array and the vortex lattice. For the antivortex lattice, the antivortices sit at the interstitial sites, experiencing weaker pinning interaction. For the vortex lattice including interstitials, the onset velocity where the lattice becomes ordered is increased by more than two orders of magnitude. Finally, for the parameters of our sample, it has been quantified that the force needed to start moving a vortex lattice is around 65% higher than the one needed to move the antivortex lattice. These findings present an important contribution to the ongoing efforts in understanding and controlling the low dissipation states in superconductors, which are as technologically relevant as the mostly considered fully superconducting state.

Acknowledgments

This work was supported by Spanish MINECO, grants FIS2008-06249 (Grupo Consolidado), Consolider CSD2007-00010 and CAM grant S2009/MAT-1726. MVM acknowledges support from FWO-Vlaanderen. Work at UCD was supported by the US NSF (DMR-1008791 and ECCS-0925626).

References

[1] Blatter G, Feigelman M V, Geshkenbein V B, Larkin A I and Vinokur V M 1994 *Rev. Mod. Phys.* **66** 1125
[2] Villegas J E, Savel'ev S, Nori F, Gonzalez E M, Anguita J V, Garcia R and Vicent J L 2003 *Science* **302** 1188
[3] Civale L, Marwick A D, Worthington T K, Kirk M A, Thompson J R, Krusinelbaum L, Sun Y, Clem J R and Holtzberg F 1991 *Phys. Rev. Lett.* **67** 648
[4] Martin J I, Jaccard Y, Hoffmann A, Nogues J, George J M, Vicent J L and Schuller I K 1998 *J. Appl. Phys.* **84** 411
[5] Velez M, Martin J I, Villegas J E, Hoffmann A, Gonzalez E M, Vicent J L and Schuller I K 2008 *J. Magn. Magn. Mater.* **320** 2547
[6] Aladyshkin A Yu, Silhanek A V, Gillijns W and Moshchalkov V V 2009 *Supercond. Sci. Technol.* **22** 053001
[7] Silhanek A V *et al* 2012 *New J. Phys.* **14** 053006
[8] Larkin A I and Ovchinnikov Y N 1979 *J. Low Temp. Phys.* **34** 409
[9] Lange M, Van Bael M J, Silhanek A V and Moshchalkov V V 2005 *Phys. Rev.* B **72** 052507
[10] Milošević M V, Yampolskii S V and Peeters F M 2002 *Phys. Rev.* B **66** 174519
Milošević M V and Peeters F M 2003 *Phys. Rev.* B **68** 094510
[11] Kramer R B G, Silhanek A V, Gillijns W and Moshchalkov V V 2011 *Phys. Rev.* X **1** 021004
[12] Kirby B J, Watson S M, Davies J E, Zimanyi G T, Liu K, Shull R D and Borcher J A 2009 *J. Appl. Phys.* **105** 07C929
[13] Davies J E, Morrow P, Dennis C L, Lau J W, McMorran B, Cochran A, Unguris J, Dumas R K, Greene P and Liu K 2011 *J. Appl. Phys.* **109** 07B909
[14] Milošević M V and Peeters F M 2004 *Phys. Rev. Lett.* **93** 267006
[15] Milošević M V and Geurts R 2010 *Physica* C **470** 791
[16] Doria M M, Gubernatis J E and Rainer D 1989 *Phys. Rev.* B **39** 9573
[17] Carcia P F, Meinhaldt A D and Suna A 1985 *Appl. Phys. Lett.* **47** 178
[18] Davies J E, Hellwig O, Fullerton E E, Denbeaux G, Kortright J B and Liu K 2004 *Phys. Rev.* B **70** 224434
[19] Velez M, Jaque D, Martín J I, Guinea F and Vicent J L 2002 *Phys. Rev.* B **65** 094509
[20] Baert M, Metlushko V V, Jonckheere R, Moshchalkov V V and Bruynseraede Y 1995 *Phys. Rev. Lett.* **74** 3269
Martín J I, Velez M, Nogues J and Schuller I K 1997 *Phys. Rev. Lett.* **79** 1929
[21] Martín J I, Velez M, Hoffmann A, Schuller I K and Vicent J L 1999 *Phys. Rev. Lett.* **83** 1022
[22] Velez M, Jaque D, Martín J I, Montero M I, Schuller I K and Vicent J L 2002 *Phys. Rev.* B **65** 104511

Silhanek A V, Van Look L, Raedts S, Jonckheere R and Moshchalkov V V 2003 *Phys. Rev.* B **68** 214504
[23] Gomez A, Gonzalez E M and Vicent J L 2012 *Supercond. Sci. Technol.* **25** 124006
[24] Morgan D J and Ketterson J B 1998 *Phys. Rev. Lett.* **80** 3614
[25] Milošević M V and Peeters F M 2005 *Europhys. Lett.* **70** 670
[26] Dinis L, Perez de Lara D, Gonzalez E M, Anguita J V, Parrondo J M R and Vicent J L 2009 *New J. Phys.* **11** 073046
[27] Milošević M V and Peeters F M 2005 *Phys. Rev. Lett.* **94** 227001
[28] Schweigert A V, Peeters F M and Singha Deo P 1998 *Phys. Rev. Lett.* **81** 2783
Kanda A, Baelus B J, Peeters F M, Kadowaki K and Ootuka Y 2004 *Phys. Rev. Lett.* **93** 257002
Milošević M V, Kanda A, Hatsumi S, Peeters F M and Ootuka Y 2009 *Phys. Rev. Lett.* **103** 217003
Xu B, Milošević M V, Lin S-H, Peeters F M and Jankó B 2011 *Phys. Rev. Lett.* **107** 057002
Cren T, Serrier-Garcia L, Debontridder F and Roditchev D 2011 *Phys. Rev. Lett.* **107** 097202
[29] Hoffmann A, Prieto P and Schuller I K 2000 *Phys. Rev.* B **61** 6958